

A multi-transition molecular line study of inward motions towards massive star-forming cores

Yan Sun^{1,2} and Yu Gao^{1*}

¹*Purple Mountain Observatory, Chinese Academy of Sciences, 2 West Beijing Road, Nanjing, Jiangsu 210008, China*

²*Graduate School of the Chinese Academy of Sciences, Beijing 100080, China*

Accepted 2008 September 19. Received 2008 September 19; in original form 2008 April 25

ABSTRACT

A multi-transition 3 mm molecular line single-pointing and mapping survey was carried out towards 29 massive star-forming cores in order to search for the signature of inward motions. Up to seven different transitions, optically thick lines $\text{HCO}^+(1-0)$, $\text{CS}(2-1)$, $\text{HNC}(1-0)$, $\text{HCN}(1-0)$, $^{12}\text{CO}(1-0)$ and optically thin lines $\text{C}^{18}\text{O}(1-0)$, $^{13}\text{CO}(1-0)$ were observed towards each source. The normalized velocity differences (δV_{CS} , δV_{HCO^+}) between the peak velocities of optically thick lines and optically thin line $\text{C}^{18}\text{O}(1-0)$ for each source were derived. Prominent inward motions are probably present in either $\text{HCO}^+(1-0)$ or $\text{CS}(2-1)$ or $\text{HNC}(1-0)$ observations in most sources. Our observations show that there is a significant difference in the incidence of blue shifted line asymmetric line profiles between $\text{CS}(2-1)$ and $\text{HCO}^+(1-0)$. The $\text{HCO}^+(1-0)$ shows the highest occurrence of obvious asymmetric feature, perhaps owing to different optical depth between $\text{CS}(2-1)$ and $\text{HCO}^+(1-0)$. $\text{HCO}^+(1-0)$ appears to be the best inward motion tracer. The mapping observations of multiple line transitions enable us to identify six strong infall candidates G123.07-6.31, W75(OH), S235N, CEP-A, W3(OH), NGC7538. The infall signature is extended up to a linear scale > 0.2 pc.

Key words: ISM: molecules – ISM: kinematics and dynamics – stars: formation – radio lines: ISM .

1 INTRODUCTION

Massive stars, once formed, dominate the luminous, kinematic, and chemical output of stars and their feedback play a dominant role in the evolution of molecular clouds and any subsequent star formation therein (Krumholz & Bonnell 2007). Despite their importance the formation of massive stars is currently an unresolved problem. The difficulties lie in their short evolution time scale and complex star-forming environment in star cluster, typically embedded in the dense cores. Two main theories for high-mass star formation are mergers of several low-mass stars (Bonnell et al. 1998), which requires a high stellar density; and accretion of materials from the circumstellar disks, which requires high accretion rate to resist radiation pressure. The latter is similar to that of low-mass star formation (Shu et al. 1987), which accompanied by outflow during the process of gravitational collapse. It appears that more observations favor the latter scenario for massive star formation (e.g. Zhang et al. 2001; Beuther et al. 2002; Patel et al. 2003; Moscadelli et al. 2005; Jiang et al. 2005; Fuller et al. 2005; Beltrán et al. 2006). Nevertheless, intermediate theories that involve

both accretions and mergers are now also quite commonly accepted (e.g. Whitney 2005; Bonnell & Bate 2006).

While accretion often can not be observed directly, its presence can be inferred from the presence of large scale infall and outflow (e.g., Klaassen & Wilson 2007). Therefore the infall motion is one of the important elements to help understand the theories of massive star formation. These motions can be studied by investigating the profiles of optically thick molecular lines, which show the blue asymmetric structure, named “blue profile”, a combination of a double peak with a brighter blue peak or a skewed single blue peak in optically thick lines (Mardones et al. 1997). Before a definite claim of collapse signature from blue profile, we should rule out all other possibilities. For example, we know double peak could be caused by two velocity components in the line of sight. To rule out this possibility we must observe optically thin line that peaks at the self-absorption dip of optically thick line (Gregersen et al. 2000; Wu & Evans 2003). Surely blue profile may also be caused by rotation or outflow. However, infall motion is the only process that would produce consistently the blue profile. Outflow and rotation only produce a blue asymmetric line profile along a particular line of sight to a source. Outflows strongly affect the line wings in the optically thick molecular line along the

* E-mail: yugao@pmo.ac.cn

outflow axes. Most infall candidates both show infall signatures and young outflows, but outflow does not seem to be responsible for blue asymmetry alone (Klaassen & Wilson 2007). Rotation might cause blue asymmetric line profile at one side of the rotation axis, but at the same time the red asymmetry could appear at the other side of the rotation axis. Mapping observation allows us to locate the center of the inflow motion and to identify dense cores that are simultaneously showing evidence for inflow motions and outflows (Wu et al. 2007).

Blue profile was detected in B335, a low-mass star formation region (Zhou et al. 1993, 1994), which is well matched by the standard model of “inside-out” gravitational collapse (Shu 1977). Subsequently, more and more blue profiles were found via large surveys towards both young stellar objects (Mardones et al. 1997; Gregersen et al. 2000) and starless cores (Lee et al. 1999, 2001, 2004; Sohn et al. 2007) in low-mass star formation regions. If massive stars are formed by accretion/collapse in a similar way as low-mass stars, blue profile of optically-thick lines should also be found towards them. Actually, these inflow signatures have been reported in many massive sources (Welch et al. 1988; Dickel & Auer 1994; Wolf-Chase & Gregersen 1997; Zhang, Ho & Ohashi 1998). Especially, several large surveys of inflow signatures in optical-thick lines towards massive young objects have been carried out, which give the important evidence of inflow/accretion/collapse (Wu & Evans 2003; Fuller et al. 2005; Klaassen & Wilson 2007; Wu et al. 2007). In these surveys, the infall velocity is found to be between 0.1 km s^{-1} and 1 km s^{-1} and the mass infall rate is estimated to be between $2 \times 10^{-4} M_{\odot}/\text{yr}$ and $10^{-3} M_{\odot}/\text{yr}$ (e.g. Fuller et al. 2005).

In this paper, we identify and study the inflow motion using several optical-thick lines including $\text{HCO}^+(1-0)$, $\text{CS}(2-1)$, $\text{HNC}(1-0)$, $\text{HCN}(1-0)$, and $^{12}\text{CO}(1-0)$. Our investigation of the profiles of optically thick molecular lines is aimed to understand two questions: (1) Is the inflow motion in massive star formation cores similar to that in low-mass star formation cores? (2) Which optical thick molecular line is the best tracer for the infall motions in massive star-forming cores? Actually, such mapping observations towards collapsing massive star-forming regions, yet are seldom, enable us to identify the most probably infall candidates. Therefore, our observational study of multiple lines in 29 high-mass star-forming regions can help better characterize the detailed properties of massive star formation in the dense cores, reveal more information about the collapsing signatures and provide some strong infall candidates.

After details of our sample selection and the related observations in the next section, the main results of this paper are presented in §3; §3.1 gives the single pointing observation results; §3.2 presents the mapping results and analyses towards the infall candidates. We discuss our observational results in §4 and summarize in §5.

2 SAMPLE & OBSERVATIONS

As a whole, the sources were selected by applying the following criteria: (1) they are associated with water masers (24 sources) or massive young stellar objects (5 sources); (2) they were included in the Spitzer Space Telescope pro-

grams before 2007; (3) source distance is less than 4 kpc. All of the 29 sources in our sample are listed in Table 1 with 22 sources (sources above the blank line in Table 1) selected from Shirley et al. 2003. To enlarge the sample, we also selected 7 sources (sources below the blank line in Table 1) from Spitzer programs that have images of massive star-forming regions. Among the 7 sources, S88 and IRAS19410 are also listed in Shirley et al. (2003) with different names as S88B and G59.78+0.06 respectively, but the source center positions are slightly different.

There is evidence that water masers are a signature of recent or ongoing high-mass star formation (e.g. Tofani et al. 1995). The first criterion of our sample selections can ensure that all sources in our sample are associated with massive star-forming regions. With high sensitivity and high spatial resolution at infrared wavelengths, the Infrared Array Camera (IRAC; Fazio et al. 2004) and Multiband Imaging Photometer for Spitzer (MIPS; Rieke et al. 2004) see through dust into the birthplaces of stars and provide new insight to directly reveal the distribution of star formation sites and their environments in which stars form. IRAC data are available to all of the targets and the MIPS data are also available for most of them. Considering the limited resolving power of the telescopes and the size of the infall region, we made some efforts to exclude distant sources. The source distances in the resulting sample are in a range from 0.6 to 4.0 kpc. The positions and distances are mainly determined from two literature search (see Table 1 for references). Most of the sample include cores of ultra-compact HII (UCHII) regions, the sample also include cores of compact HII (CHII) and HII regions.

Our observations were carried out using the 14 m telescope of Purple Mountain Observatory (PMO) in Delingha, China. The position-switch mode was used, the pointing accuracy is estimated to be better than $9''$. One SIS receivers operating at $\sim 110 \text{ GHz}$ were used in the observations along with an acoustic-optic spectrometer (AOS) back end with 1024 channels. The standard chopper wheel calibration was used during the observations to get the antenna temperature, T_A^* , which has been corrected for atmospheric absorption. The typical system temperatures T_{sys} is about 250-350 K. At central source position, the accumulated integration time towards each source is larger than 10 minutes and the signal-to-noise ratio is larger than 10. We carried out our mapping observation only towards strong emission ($T_A^* > 0.5 \text{ K}$ in $\text{HCO}^+(1-0)$ and $\text{CS}(2-1)$) sources with line asymmetry for the sake of the observational efficiency. The positions of CO emission peak (which were marked in Table 1) have the highest priority in further $\text{HCO}^+(1-0)$ and $\text{CS}(2-1)$ observations.

The mapping step is $30''$ for $\text{CS}(2-1)$, $\text{HCO}^+(1-0)$, and $1'$ (\sim beam size, for our source distance, corresponding to linear resolution between 0.16 pc and 1.07 pc) for $^{12}\text{CO}(1-0)$, $^{13}\text{CO}(1-0)$, $\text{C}^{18}\text{O}(1-0)$. To complement our study, we have also used some data from Ma, Gao, & Wu (2008 in prep.) including $\text{CS}(2-1)$, $\text{HCO}^+(1-0)$, $\text{HNC}(1-0)$ and $\text{HCN}(1-0)$ mapping data. These ten sources are marked with \bullet in Table 1 and they were observed with the SEQUOIA on the former Five Colleges Radio Astronomy Observatory (FCRAO) 14m telescope with a $25''$ on-the-fly mapping step. The detailed observation log is listed in Table 2.

The spectral data were reduced and analyzed with

Table 1. Source positions and rms T_A^* noise levels in spectra (with channel width 50 KHz).

source	RA. (2000.0)	Decl. (2000.0)	Distance (kpc)	HII?	centroid ($'$)	CS 2-1 K	HCO ⁺ 1-0 K	C ¹⁸ O 1-0 K	Map Size CS 2-1($'$)	Map Size HCO ⁺ 1-0($'$)
G123.07-6.31	00:36:47.51	+63:29:02.08	2.2	HII	(0,0)	0.038	0.068	0.053	3×3	3×3
●W3(OH)	02:27:04.69	+61:52:25.54	1.95	UCHII	(0,0)	0.083	0.060	0.038	7×7	7×7
S231	05:39:12.91	+35:45:54.05	2.3	...	(0,0)	0.061	0.084	0.072	2×2	...
S235	05:40:53.32	+35:41:48.76	1.6	HII	(0,0)	0.058	0.087	0.093	2×2	...
S252A	06:08:35.41	+20:39:02.96	1.5	HII	(0,0)	0.038	0.081	0.037	2×2	...
●S255	06:12:53.72	+17:59:22.03	1.3	UCHII	(0,0)		0.115	0.066		7×7
G19.61-023	18:27:38.84	-11:56:27.44	4.0	CHII	(0,0)	0.039	0.034	0.072
G20.08-0.13	18:28:09.88	-11:28:48.17	3.4	UCHII	(0,0)	0.040	0.046	0.086
G24.49-0.04	18:35:05.34	-07:31:26.98	3.5	...	(0,0)			0.106
●W44	18:53:18.50	+01:14:56.65	3.7	CHII	(0,0)	0.092	0.104	0.075	7×7	7×7
S76E	18:56:10.43	+07:53:14.11	2.1	HII	(0,0)	0.040	0.061	0.092	3.5×3	...
G35.58-0.03	18:56:22.57	+02:20:27.75	3.5	UCHII	(0,0)	0.038	0.043	0.076	2×2	...
G35.20-0.74	18:59:12.73	+01:40:40.75	3.3	HII	(0,0)	0.027	0.027	0.091
OH43.80-0.13	19:11:54.27	+09:35:55.38	2.7	UCHII	(0,0)	0.039	0.052	0.078	2×2	...
●S87	19:46:20.45	+24:35:34.41	1.9	UCHII	(0,0)	0.111	0.088	0.076	7×7	7×7
●S106	20:27:25.74	+37:22:51.82	0.6	UCHII	(0,0)	0.070	0.079	0.030	7×7	7×7
●W75N	20:38:36.93	+42:37:37.52	3.0	UCHII	(0,0)	0.091	0.071	0.047	7×7	7×7
DR21S	20:39:00.80	+42:19:29.84	3.0	UCHII	(0,0)	0.038	0.076	0.137	2×2	2×2
●W75(OH)	20:39:01.01	+42:22:49.84	3.0	...	(0,0)	0.118	0.090	0.085	7×7	7×7
●BFS11-B	21:43:06.68	+66:07:04.11	2.0	...	(0,0)	0.085	0.107	0.065	7×7	7×7
●Cep-A	22:56:18.14	+62:01:46.35	0.7	UCHII	(0,0)	0.117	0.089	0.024	7×7	7×7
●NGC7538	23:13:44.86	+61:26:50.71	2.8	UCHII	(0,0)	0.232	0.073	0.032	7×7	7×7
AFGL4029	03:02:00.00	+60:33:49.00	2.2	UCHII	(-3,-4)	0.054	0.061	0.063	2.5×2.5	2.5×3
AFGL5142	05:30:48.00	+33:47:53.80	1.8	HII	(0,0)	0.041	0.073	0.040	2×2	2×2
S235N	05:41:00.00	+35:48:04.00	1.6	...	(6,2)	0.042	0.068	0.053	2×2	2×2
G192	05:58:17.07	+16:31:58.00	2.0	UCHII	(-1,0)	0.025	0.052	0.070	2×2	...
IRAS19410	19:43:11.00	+23:44:06.00	2.2	UCHII	(0,0)	0.031	0.040	0.028	3×3	2×2
S88	19:46:43.00	+25:12:14.00	2.1	UCHII	(1,1)	0.047	0.072	0.059	2×2	2×2
IRAS20126	20:14:25.80	+41:13:33.00	1.7	...	(0,0)	0.039	0.114	0.094	3.5×3	...

NOTE.-positions and distances of sources above the blank line are from Shirley et al. 2003, except for W3(OH) and S106. The distance of W3(OH) is from Xu et al. 2006. The distance of S106 is from Eiroa Elasser & Lahulla 1979; Ridge et al. 2003. For the last eight sources, positions are from Spitzer observing center, distances are from Carral et al. 1999, except for IRAS19410. The distance of IRAS19410 is from Xu et al. 2007. Note that S235 has a relatively extended distribution, the north region was indicated by S235N. Centroid is the ¹³CO(1-0) peak position of each source. Columns 7,8,9 are rms T_A^* noise levels towards ¹³CO(1-0) peak position of each source in CS(2-1), HCO⁺(1-0), C¹⁸O(1-0) respectively. Symbol ... in the columns 10 and 11 denoted only single point was observed.

Table 2. Observed lines and telescope parameters.

Line	Data (UT)	Frequency (GHZ)	Telescope	FWHM (arcsec)	η_{mb}^a	Δv (km s ⁻¹)	$T_{sys}(T_A^*)$ K
¹² CO(1-0)	2005 Nov	115.271204	PMO 14m	55	0.72	0.37	
	2006 Nov	115.271204	PMO 14m	55	0.57	0.37	
¹³ CO(1-0)	2005 Nov	110.201353	PMO 14m	55	0.72	0.11	200-350
	2006 Nov	110.201353	PMO 14m	55	0.57	0.11	
¹⁸ CO(1-0)	2005 Nov	109.782173	PMO 14m	55	0.72	0.12	
	2006 Nov	109.782173	PMO 14m	55	0.57	0.12	
HCO ⁺ (1-0)	2007 Jun	89.1885260	PMO 14m	55	0.62	0.14	280-400
	2005 May	89.1885180	FCRAO 14m	57	0.53	0.16	160-210
CS(2-1)	2007 May	97.9809530	PMO 14m	55	0.62	0.13	160-250
	2005 May	97.9810070	FCRAO 14m	54	0.49	0.15	120-210
HNC(1-0)	2005 May	90.6635720	FCRAO 14m	57	0.53	0.16	160-210
HCN(1-0)	2005 May	88.6318473	FCRAO 14m	57	0.53	0.17	120-200

^a η_{mb} is the main beam efficiency.

CLASS and IDL software. Linear baselines were removed from all spectra. The rms levels for each spectrum at the CO emission peak are also listed in Table 1. The complete description of our multiple molecular line observations and all data presentation will be given in a forthcoming paper (Sun & Gao 2008 in prep.)

There is little overlap in the samples of previous observational search for infall signatures, particularly the mapping studies. Two major surveys of inflow motion observations that have some source overlaps with our sample are Wu

& Evans (2003) and Klaassen & Wilson (2007). There are fifteen sources that overlap between our HCO⁺(1-0) mapping observations and that of single-pointing HCN(3-2) observation of Wu & Evans (2003). Yet, only five sources in our sample overlap with the single-pointing HCO⁺(4-3) observation of Klaassen & Wilson (2007).

3 ANALYSIS & RESULTS

All targets are detected in $\text{HCO}^+(1-0)$, $\text{CS}(2-1)$, $\text{C}^{18}\text{O}(1-0)$, $^{12}\text{CO}(1-0)$, $^{13}\text{CO}(1-0)$, except for G24.49-0.04 owing to a wrong frequency setup (a wrong V_{LSR} was taken). Most sources are pretty strong with T_{A}^* of $\text{HCO}^+(1-0)$, $\text{CS}(2-1)$ mainly in a range of 1-4.5 K. But several sources (G19.61-023, G20.08-0.13, G35.58-0.03, G35.20-0.74) show fairly weak emission ($T_{\text{A}}^* < 0.3$ K) in $\text{HCO}^+(1-0)$, and one source (G35.20-0.74) shows quite weak emission ($T_{\text{A}}^* < 0.2$ K) in $\text{CS}(2-1)$. Among the 29 dense cores observed, S255 shows a very marginal detection in CS emission and S76E has two velocity components in both $\text{C}^{18}\text{O}(1-0)$ and $^{13}\text{CO}(1-0)$ and is difficult to determine the systematic velocity. Therefore, these sources (G24.49-0.04, S255, S76E) are excluded from the following analysis. We only give the results derived from $\text{CS}(2-1)$ and $\text{HCO}^+(1-0)$ as optically thick spectral lines towards 26 sources below since only ten sources have both $\text{HCN}(1-0)$ and $\text{HNC}(1-0)$ observations.

3.1 Blue profile identification

To quantify the blue asymmetry of a line, we use an asymmetry parameter δV (pioneered by Mardones et al. 1997) defined as the difference between the peak velocities of an optically thick line $V(\text{thick})$ and an optically thin line $V(\text{thin})$ in units of the optically thin line FWHM (Full Width at Half Maximum) $dV(\text{thin})$: $\delta V = \frac{V(\text{thick}) - V(\text{thin})}{dV(\text{thin})}$. Mardones et al. (1997) adopted a criterion $\delta V < -0.25$ to indicate blue asymmetry and $\delta V > 0.25$ to indicate red asymmetry. They chose the threshold value 0.25 at about 5 times the typical rms error in δV in order to exclude the random contributions (Mardones et al. 1997). We use the same criterion for consistency with their analysis. Because of the asymmetric profiles for many of optical-thick lines, they cannot be fitted by Gaussian function, the peaks of the line profiles of $\text{CS}(2-1)$, $\text{HCO}^+(1-0)$, and $\text{HNC}(1-0)$ are identified with the highest flux by cursor. The uncertainties of the velocities and the antenna temperatures at these peaks were estimated by several measurements and the baseline fitting noises. The optically thin line (C^{18}O) shows an ideal Gaussian profile and is fitted by the Gaussian function to obtain the peak velocity and FWHM. All these parameters towards the $^{13}\text{CO}(1-0)$ peak position are listed in Table 3 which includes the peak velocities of $\text{CS}(2-1)$, $\text{HCO}^+(1-0)$, $\text{C}^{18}\text{O}(1-0)$, the FWHM of $\text{C}^{18}\text{O}(1-0)$, the calculated asymmetry parameter δV of $\text{CS}(2-1)$ and $\text{HCO}^+(1-0)$, and the uncertainties of these parameters (in the parentheses) for all sources.

The blue profile caused by infall motion also requires $T_{\text{A}}^*(B)/T_{\text{A}}^*(R) > 1 + \sigma$ (i.e., the blue peak is stronger than the red peak, hereafter $T_{\text{B}}/T_{\text{R}} \equiv T_{\text{A}}^*(B)/T_{\text{A}}^*(R)$). These ratios of $\text{CS}(2-1)$ and $\text{HCO}^+(1-0)$ towards the $^{13}\text{CO}(1-0)$ peak position are available in Table 3. The peak antenna temperatures of $\text{CS}(2-1)$ and $\text{HCO}^+(1-0)$ towards each source are also listed in table 3 columns 8 and 10, respectively. Based on the methods that we used to derive the ratio of $T_{\text{B}}/T_{\text{R}}$, the sources can be classified into three groups: (1) sources show obvious two peaks, we can accurately measure the ratio of $T_{\text{B}}/T_{\text{R}}$; (2) sources with asymmetry profiles but do not show obviously two peaks (both blue and red), thus only one peak (either blue or red velocity offset) can be identified. We simply chose the same velocity offset to the systematic veloc-

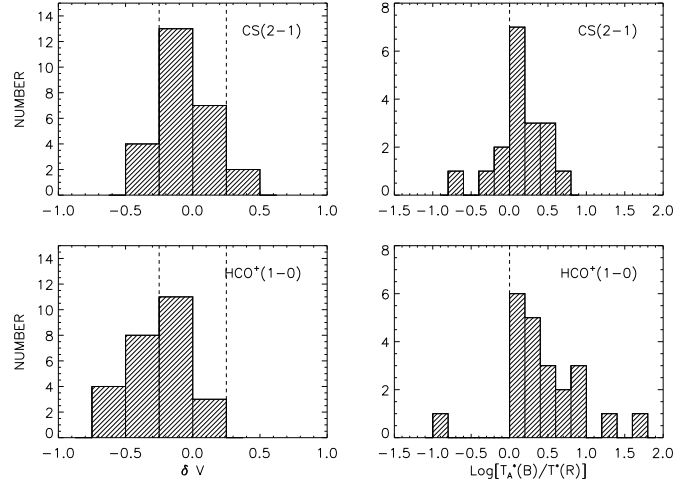


Figure 1. Distribution of δV (left, the line asymmetry parameter) and $\log[T_{\text{A}}^*(B)/T_{\text{A}}^*(R)]$ (right, ratio of blue to red peak intensity). The top and bottom panels show results from $\text{CS}(2-1)$ and $\text{HCO}^+(1-0)$ respectively.

ity as the other peak, so $T_{\text{B}}/T_{\text{R}}$ can not be exactly derived. We mark “~” before such sources; (3) sources almost don’t show any asymmetry, neither the red nor blue component can be identified, so the intensity ratio $T_{\text{B}}/T_{\text{R}}$ was flagged with “...”.

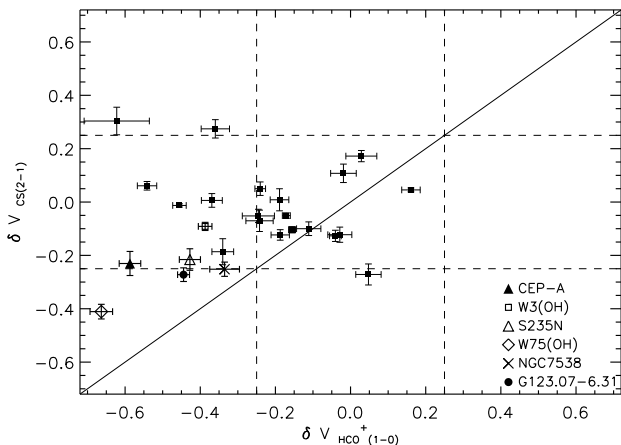
In our sample, four blue profiles were identified in $\text{CS}(2-1)$, fourteen blue profiles were identified by $\text{HCO}^+(1-0)$, three sources show blue profiles both in $\text{CS}(2-1)$ and $\text{HCO}^+(1-0)$ spectra. Within the error bars, the parameters (δV , $T_{\text{B}}/T_{\text{R}}$) of several sources (W44, G192, G35.20-0.74, S88) are approaching the criterion, so they are possible candidates of the blue profiles or red profiles and are marked with “?” in Table 3. Note that S87 and G35.20-0.74 show different asymmetry between $\text{CS}(2-1)$ and $\text{HCO}^+(1-0)$. S87 also shows different asymmetry at different positions. At offsets ($0''$, $25''$), ($0''$, $-25''$), ($25''$, $0''$), ($-25''$, $0''$), it shows red asymmetry, blue asymmetry, no asymmetry, blue asymmetry in $\text{HCO}^+(1-0)$ and red asymmetry, no asymmetry, red asymmetry, red asymmetry in $\text{CS}(2-1)$, respectively. These might suggest a complicated kinematics in the mapped regions in S87 (c.f. Xue & Wu 2008, where they claimed that the asymmetric line profiles in S87 should result from two clouds at slightly different velocities). Figure 1 presents the statistics of the asymmetry parameters measured towards the $^{13}\text{CO}(1-0)$ peak position of the 26 sources observed in both $\text{HCO}^+(1-0)$ and $\text{CS}(2-1)$ mentioned before. It’s clear that the blue profile predominance was shown, particularly in $\text{HCO}^+(1-0)$. Because infall is the only process that would produce consistently the blue profile, its predominance indicates that the infall motions are really present in massive star-forming regions. A comparison of the asymmetry parameter δV in $\text{CS}(2-1)$ and $\text{HCO}^+(1-0)$ is shown in Figure 2, which shows weak correlation between δV in the two molecular lines. As noted above, G35.20-0.74 and S87 show different asymmetry between $\text{CS}(2-1)$ and $\text{HCO}^+(1-0)$ and also greatly affect the correlation between δV of the two lines. Generally, there are more sources with blue asymmetric profiles in $\text{HCO}^+(1-0)$ line than those in $\text{CS}(2-1)$. We will further discuss the difference between the two lines in §4.

Table 3. The Derived line parameters and profiles of the observed sources. Quantities in parentheses give the uncertainties in units of 0.01.

source ^a	V_{thick} CS 2-1 km s ⁻¹	V_{thick} HCO ⁺ 1-0 km s ⁻¹	V_{thin} C ¹⁸ O 1-0 km s ⁻¹	ΔV C ¹⁸ O 1-0 km s ⁻¹	δv CS 2-1	δv HCO ⁺ 1-0	T_{peak} CS 2-1 K	T_B/T_R CS 2-1	T_{peak} HCO ⁺ 1-0 K	T_B/T_R HCO ⁺ 1-0	profile ^b
*g123.07-6.31	-18.04(04)	-18.35(01)	-17.55(02)	1.80(04)	-0.27(03)	-0.44(02)	1.52	1.54	2.95	1.79	B,B,B
*W3(OH)	-47.53(06)	-48.76(07)	-47.15(02)	4.16(05)	-0.09(02)	-0.39(02)	3.73	~1.08	2.87	2.34	N,B,B
S231	-17.14(03)	-17.33(01)	-16.76(03)	3.66(07)	-0.10(01)	-0.16(01)	1.31	~1.08	2.18	~1.09	N,N,R
S235	-16.83(09)	-17.30(04)	-16.85(04)	2.38(09)	0.01(04)	-0.19(02)	2.12	...	2.52	~1.47	N,N,N
S252A	8.95(05)	8.60(10)	8.53(01)	2.44(03)	0.17(02)	0.03(04)	1.76	~0.91	1.56	...	N,N,R
G19.61-0.23	42.79(12)	40.31(06)	42.75(12)	6.61(34)	0.01(03)	-0.37(03)	0.62	...	0.32	~1.58	N,B,N
G20.08-0.13	41.79(14)	41.29(07)	42.13(13)	4.83(39)	-0.07(04)	-0.17(03)	0.53	...	0.29	~1.53	N,N,~
◇W44	58.02(13)	56.51(07)	57.76(02)	5.20(04)	0.05(03)	-0.24(01)	3.27	...	2.96	~4.96	N,B?B
G35.58-0.03	53.29(04)	54.00(15)	53.01(02)	6.16(06)	0.05(01)	0.13(01)	1.01	~0.94	0.34	~0.39	N,N,N
G35.20-0.74	37.50(04)	36.25(09)	37.09(05)	1.35(09)	0.30(05)	-0.62(09)	0.16	~0.79	0.17	~1.05	R?B?~
OH43.80-0.13	43.88(06)	43.82(12)	44.41(12)	5.30(21)	-0.10(03)	-0.11(03)	0.72	~1.19	0.80	~1.20	N,N,~
S87	23.35(06)	21.20(07)	22.42(09)	3.39(16)	0.27(03)	-0.36(04)	2.15	0.47	3.28	1.26	R,B,~
◇S106	-1.47(12)	-1.85(07)	-1.01(01)	2.47(03)	-0.19(05)	-0.34(03)	1.74	~1.58	1.63	~1.33	N,B,~
W75N	9.25(07)	9.55(05)	9.69(02)	3.47(05)	-0.13(02)	-0.04(02)	3.30	~1.00	2.97	...	N,N,R
DR21S	-2.59(03)	-4.47(05)	-2.78(04)	3.12(09)	0.06(02)	-0.54(03)	2.88	...	2.41	1.35	N,B,B
*W75(OH)	-4.28(07)	-5.03(07)	-3.06(03)	2.97(07)	-0.41(03)	-0.66(03)	4.36	1.88	4.11	2.00	B,B,B
BFS11-B	-10.05(05)	-10.25(05)	-10.22(02)	1.58(08)	0.11(03)	-0.02(03)	1.50	~1.25	2.35	...	N,N,~
*Cep-A	-11.44(16)	-12.71(10)	-10.62(01)	3.56(03)	-0.23(05)	-0.59(03)	2.43	1.19	2.29	2.29	N,B,B
*NGC7538	-57.36(14)	-57.81(21)	-56.00(03)	5.40(07)	-0.25(03)	-0.34(04)	5.16	~1.48	3.96	~3.42	B,B,~
AFGL4029	-38.35(01)	-38.49(03)	-38.08(04)	2.19(10)	-0.12(02)	-0.19(02)	1.89	~1.19	1.82	~1.22	N,N,~
AFGL5142	-3.51(02)	-3.84(02)	-3.37(02)	2.75(04)	-0.05(01)	-0.17(01)	3.67	...	3.71	~1.31	N,N,~
*S235N	-20.23(10)	-20.83(04)	-19.62(05)	2.83(11)	-0.22(04)	-0.43(03)	1.08	~1.28	1.98	2.68	N,B,~
G192	5.61(06)	6.28(05)	6.18(05)	2.10(10)	-0.27(04)	0.05(03)	0.31	~1.63	0.70	1.09	B?N,~
IRAS19410	22.54(01)	21.50(04)	22.57(01)	2.35(02)	-0.01(01)	-0.46(02)	1.82	...	1.50	1.06	N,B,B
S88	21.90(06)	21.38(11)	22.04(03)	2.69(06)	-0.05(02)	-0.25(04)	0.91	...	2.43	2.18	N,B?R
IRAS20126	-3.88(03)	-3.65(05)	-3.58(06)	2.45(16)	-0.12(03)	-0.03(03)	1.06	~1.16	2.24	...	N,N,~

^a Sources marked with ◇ and * are considered to be probably and strong infall candidates, respectively.

^b Profile is judged from our CS(2-1), HCO⁺(1-0) observations and HCN(3-2) observation of Wu & Evans (2003), respectively. B denotes blue profile, R denotes red profile, N denotes neither blue nor red, ~ denotes no HCN(3-2) data


Figure 2. Comparison of the measured asymmetry in HCO⁺(1-0) and CS(2-1). The dashed lines mark $|\delta V| = 0.25$ and the line of equality is shown in solid.

3.2 Infall candidates

The mapping observations of multiple transitions could offer detailed investigation to provide strong evidence on whether the core is an infall candidate. It has been widely accepted that the infall candidates must show obvious blue profile at least in one optically thick line, no red profile in other infall tracers and no spacial difference in the mapping observation. Based on all of these, we have found three probable infall candidates (S106, W44, IRAS19410) and six strong

infall candidates (G123.07-6.31, W75(OH), S235N, CEP-A, W3(OH), NGC7538). The strong infall candidates are marked in Table 3 and Figure 2.

Figures 3-8 show the HCO⁺(1-0) mapping observations towards the six most strong infall candidates (Figs.4-7 are presented with only central parts of the HCO⁺(1-0) maps). Most of the data show obvious asymmetric profiles and all of spectral lines observed towards the ¹³CO(1-0) emission peak position. The six infall candidates show consistent blue profile in at least one optically thick spectral line. Most of them show high velocity wing emissions both in HCO⁺(1-0) and ¹²CO(1-0). These might suggest that besides infall motions outflows are also present in the infall candidates. Klaassen & Wilson (2007) also found that seven out of their nine infall candidates show SiO detections. All these confirm that inflow was often accompanied by outflow in the process of massive star forming process. In these strong infall candidates a large scale blue asymmetry was present. From our maps we estimated the extent of the infall signature to be up to 2' × 2' (at least 0.66 pc for G123.07-6.31, 0.59 pc for W3(OH), 1.03 pc for W75(OH), 0.21 pc for CEP-A, 0.84 pc for NGC7538, and 0.34 pc for S235N).

We here choose G123.07-6.31 as a typical example of infall candidate to illustrate our observations (Figure 3). In Figure 3a, a signature of extended inward motions were detected in all the mapping region of our HCO⁺(1-0) observation, detailed analysis was needed to better understand the spatial variation of the infall speed of the core. Figure 3b shows all of molecular lines observed towards the maser site (0,0), and outer region of the core (1',-1'). Obvious blue asymmetry is presented in both CS(2-1) and HCO⁺(1-0).

Along $\Delta\text{decl.} = 0$ the position-velocity (P-V) diagram of $\text{HCO}^+(1-0)$ shows strong blue asymmetry (Figure 3c top) while the P-V diagram of $\text{C}^{18}\text{O}(1-0)$ doesn't show any asymmetry (Figure 3c bottom).

A noticeable feature in Figure 9 is that the $\text{HCO}^+(1-0)$ lines generally have higher intensity ratios T_B/T_R than that in $\text{CS}(2-1)$ for the six infall candidates; typically ~ 2.2 for $\text{HCO}^+(1-0)$ and ~ 1.4 for $\text{CS}(2-1)$. The difference is significantly larger than any possible errors produced in determining T_B/T_R . A simple analytic model for collapse (Myers et al. 1996) predicted that the ratio of blue to red component (T_B/T_R) increases with infall speed (V_{in}), which assumes that the cloud consists of two uniform paralleled components without rotation and the infall speed of the gas is less than the velocity dispersion σ . Thus, it is likely that HCO^+ and CS trace different infall speeds given their different intensity ratios. This also suggests that the infall speeds derived from $\text{HCO}^+(1-0)$ and $\text{CS}(2-1)$ might be different. Of course, we do not expect the derived infall speeds to be same because different infall tracers might trace different spatial components of the clouds along the line of sight. From the mapping observations, it is obvious that the infall speed is also different in different spatial components perpendicular to the line of sight. Thus, these two lines do not necessarily provide duplicate information. Rotation might cause blue asymmetric line profile at one side of the rotation axis, but at the same time the red asymmetry could appear at the other side of the rotation axis. Based on this argument, we could exclude the rotation as the main contributor. We did not do any model fit towards these sources in this paper, some modelling efforts will need to be developed in order to derive the infall motion and mass infall rate in future work.

4 DISCUSSION

As presented in the previous section, an obvious asymmetry parameter difference was shown between $\text{HCO}^+(1-0)$ and $\text{CS}(2-1)$ in Figs. 2 and 9. $\text{HCO}^+(1-0)$ line seems to be a better tracer for the study of infall motion compared with $\text{CS}(2-1)$. In general, the characteristic blue profile will appear only if the molecular line tracer has a suitable optical depth and critical density. Both $\text{HCO}^+(1-0)$ and $\text{CS}(2-1)$ are optically thick lines, but $\text{HCO}^+(1-0)$ is more opaque than $\text{CS}(2-1)$ (Evans 2003). The critical density of the two lines is also different. At $T_k=100\text{K}$, the critical density of $\text{CS}(2-1)$ is $3.9 \times 10^5 \text{cm}^{-3}$ (Evans 1999), while the critical density of $\text{HCO}^+(1-0)$ is $1.9 \times 10^5 \text{cm}^{-3}$ (Evans 1999; cf. $5.0 \times 10^4 \text{cm}^{-3}$ Fuller et al. 2005). A natural explanation for the asymmetry parameter difference between $\text{CS}(2-1)$ and $\text{HCO}^+(1-0)$ is that infall motions are more easily detected in the lower density outer region of the dense core. In the denser regions, the infall motions might be significantly decelerated by thermal pressures, outflows, and other feedbacks from the massive young objects.

Nevertheless, $\text{HCN}(3-2)$ has a much higher critical density ($6.8 \times 10^7 \text{cm}^{-3}$ at $T_k = 100 \text{K}$) than that of $\text{CS}(2-1)$, yet it still shows a high inflow motion detection rate (Wu & Evans 2003). In the fifteen sources that overlap between our survey and that of Wu & Evans (2003), the profiles derived from $\text{HCO}^+(1-0)$ are more consistent with that derived from $\text{HCN}(3-2)$ than that of $\text{CS}(2-1)$ (see Table 3.). The difference

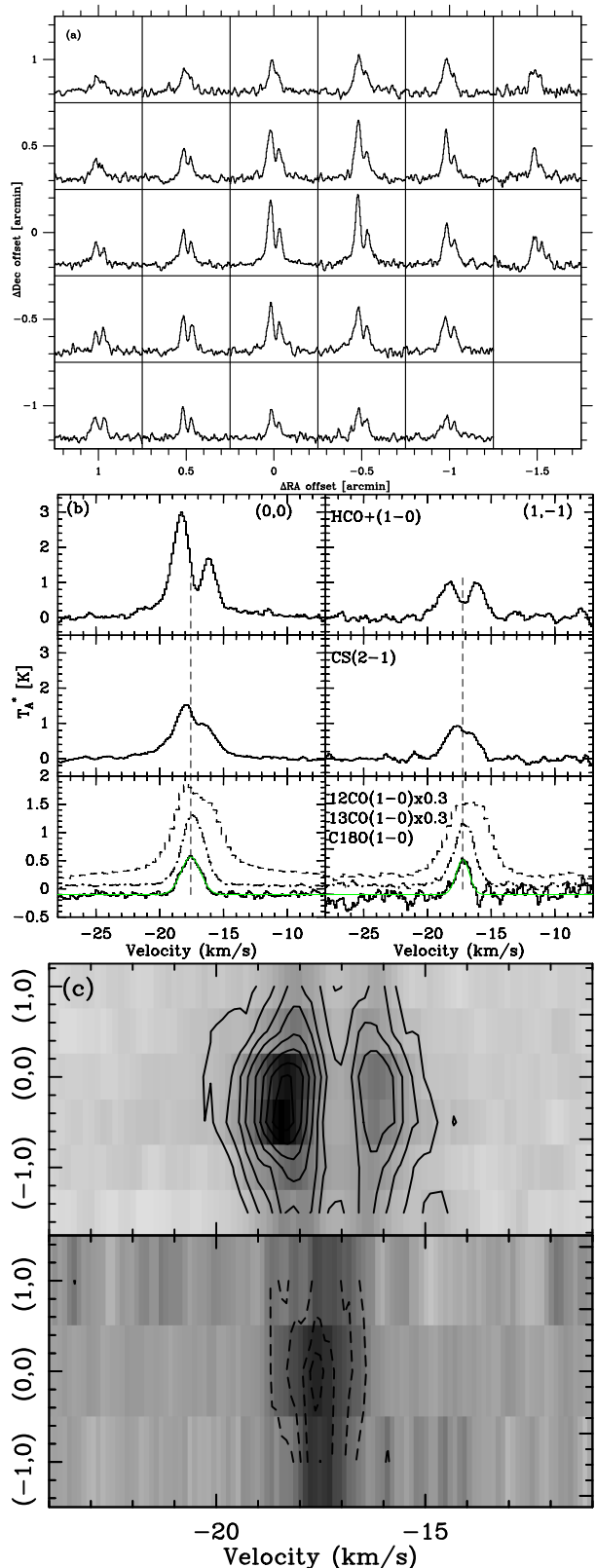


Figure 3. G123.07-6.31 (a) $\text{HCO}^+(1-0)$ map grid. (b) Spectral towards (0,0) (left), and (1',-1') (right) the dashed line marked the source systemic velocity which was derived from gauss fit of $\text{C}^{18}\text{O}(1-0)$. (c) Position-velocity diagrams of optically thick $\text{HCO}^+(1-0)$ line (top) and optically thin $\text{C}^{18}\text{O}(1-0)$ line (bottom), contour levels are 0.4K ($> 3\sigma$), 0.7K, 1.0K, 1.3K, 1.7K, 2.1K, 2.5K, 2.9K and 0.3K ($> 3\sigma$), 0.5K, 0.7K, 0.8K, 0.9K, respectively.

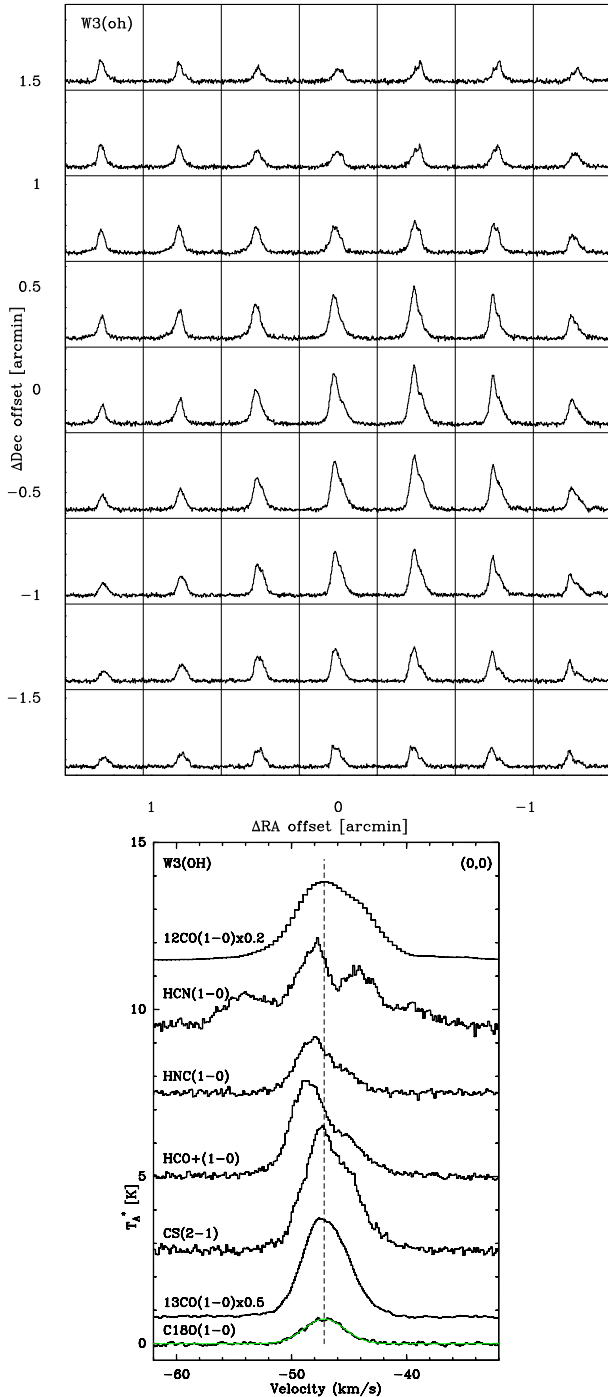


Figure 4. W3(OH), the top and bottom panels present the center parts that show obvious asymmetric profiles of $\text{HCO}^+(1-0)$ map grid and all of spectral lines observed towards (0,0), respectively. In the top panel, the velocity scale ranges from -62 km s^{-1} to -32 km s^{-1} the same as the bottom panel, the temperature scale ranges from -0.5 K to 4.4 K .

between the optical depth of the two molecular lines might be the more important reason than the difference in the critical density of the two lines. A recent model about blue asymmetry in low-mass star-forming region suggests that the line asymmetry is strongly dependent on the abundance

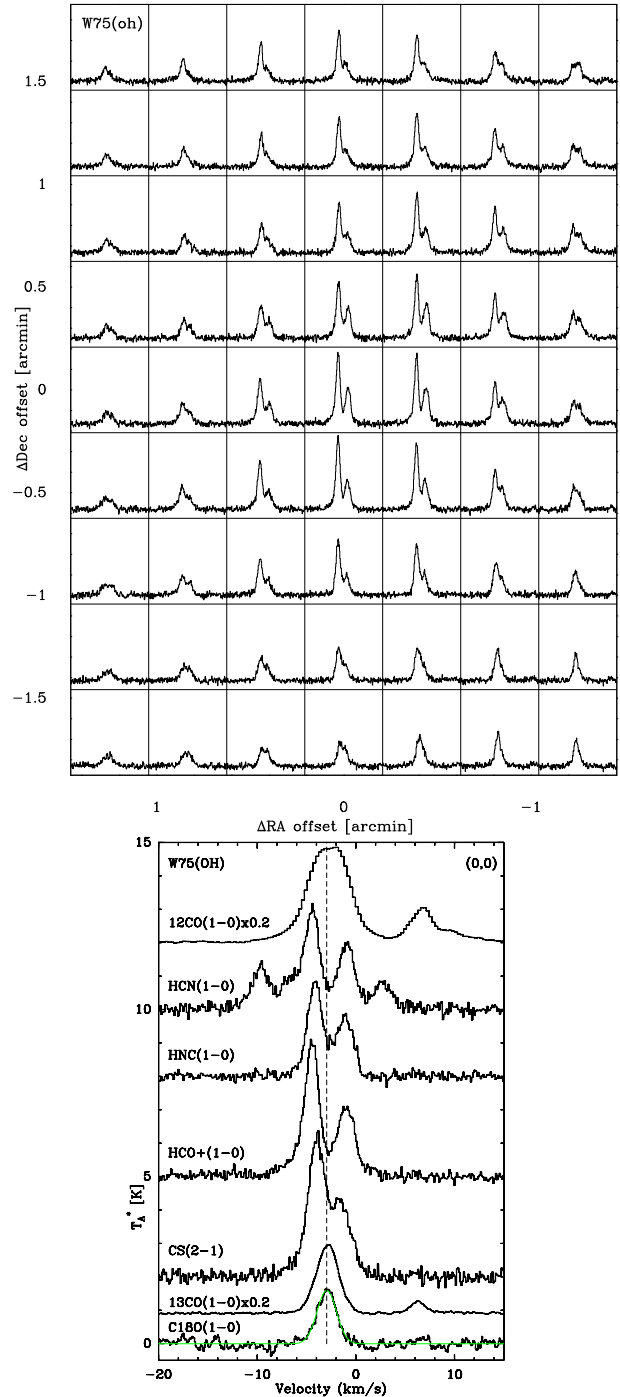


Figure 5. W75(OH), the top and bottom panels present the center parts that show obvious asymmetric profiles of $\text{HCO}^+(1-0)$ map grid and all of spectral lines observed towards (0,0), respectively. In the top panel, the velocity scale ranges from -20 km s^{-1} to 15 km s^{-1} the same as the bottom panel, the temperature scale ranges from -0.5 K to 4.4 K .

distribution (Tsamis et al. 2008), which is proportional to the optical depth.

In the fifteen overlap sources, more blue and red profiles were presented by Wu & Evans (2003) than that of ours. Their $\text{HCN}(3-2)$ observations were carried out in a single pointing toward dense cores using the CSO 10.4m telescope

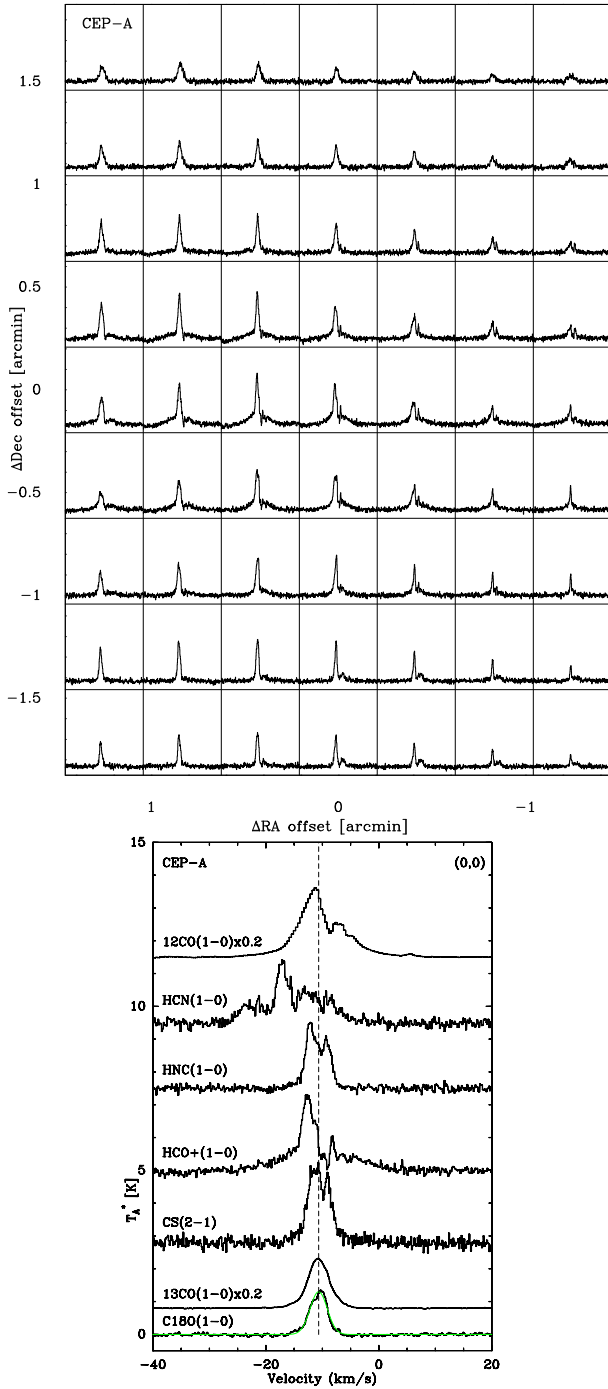


Figure 6. CEP-A, the top and bottom panels present the center parts that show obvious asymmetric profiles of $\text{HCO}^+(1-0)$ map grid and all of spectral lines observed towards (0,0), respectively. In the top panel, the velocity scale ranges from -40 km s^{-1} to 20 km s^{-1} the same as the bottom panel, the temperature scale ranges from -0.5 K to 4.4 K .

with resolution about $28''$. The higher spatial resolution enables them to better resolve the inner small regions of inward motions. In particular, G19.61-0.23 shows blue profile in both $\text{HCO}^+(1-0)$ of our results and $\text{HCO}^+(4-3)$ of the JCMT observations with resolution about $15''$ (Klaassen & Wilson, 2007), but no obvious asymmetry in $\text{HCN}(3-2)$ (Wu & Evans 2003). S88 shows blue profile in $\text{HCO}^+(1-0)$ over a

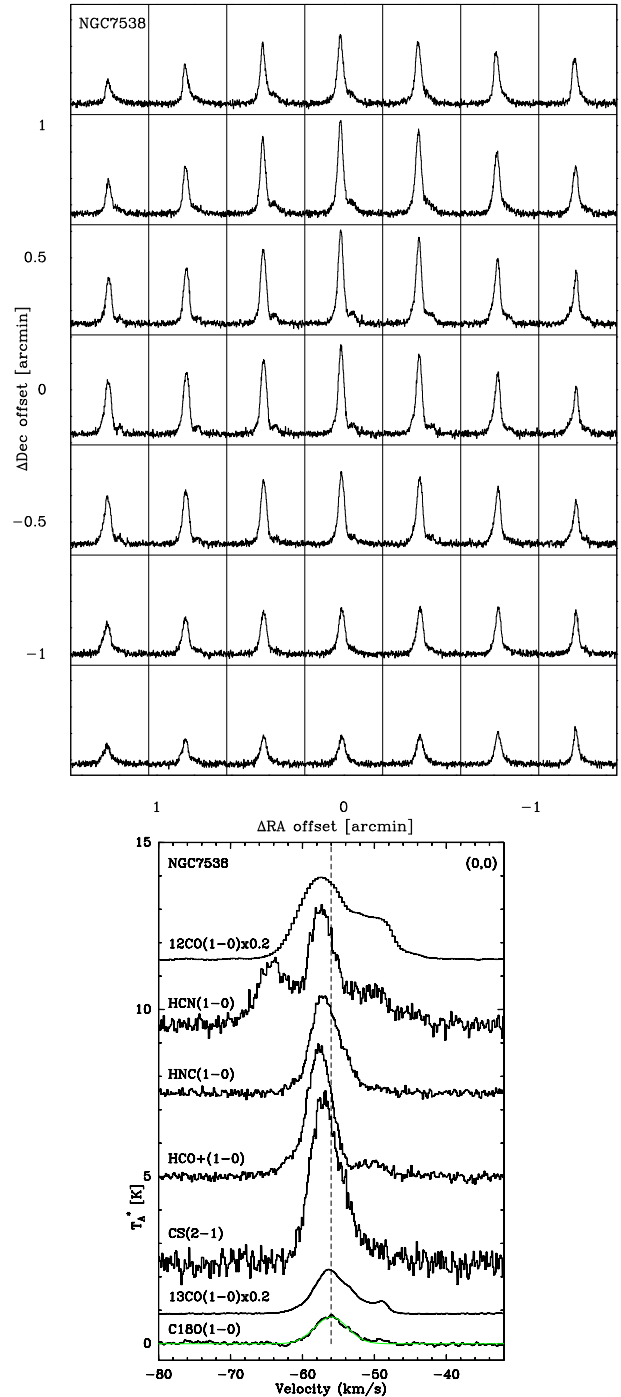


Figure 7. NGC7538, the top and bottom panels present the center parts that show obvious asymmetric profiles of $\text{HCO}^+(1-0)$ map grid and all of spectral lines observed towards (0,0), respectively. In the top panel, the velocity scale ranges from -80 km s^{-1} to -32 km s^{-1} the same as the bottom panel, the temperature scale ranges from -0.5 K to 4.4 K .

$2' \times 2'$ mapping region in our observations whereas it shows red profile in a single pointing $\text{HCN}(3-2)$ observation of Wu & Evans (2003), yet it shows no obvious asymmetry in single pointing $\text{HCO}^+(4-3)$ observation of Klaassen & Wilson (2007). In a recent survey, Fuller et al. (2005) also found that the detection rate of infall motion decreases with in-

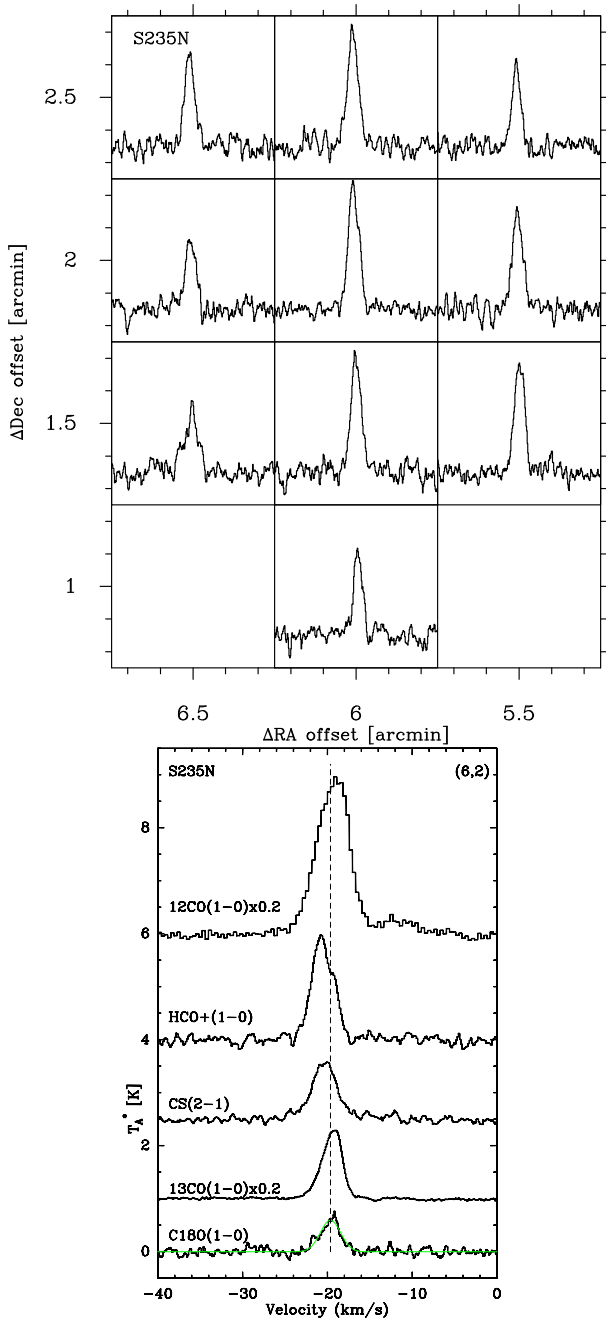


Figure 8. S235N, the top and bottom panels present $\text{HCO}^+(1-0)$ map grid and all of spectral lines observed towards $(6', 2')$, respectively. In the top panel, the velocity scale ranges from -40 km s^{-1} to 0 km s^{-1} the same as the bottom panel, the temperature scale ranges from -0.5 K to 2 K .

creasing source distance. In short, the source distance, half power beam width (HPBW) of the molecular transition line probes, and the size scale of infall region could all affect the infall detection rate.

Even though our observations (resolution $\sim 1'$) did not have the resolving power to probe a linear scale $< 0.16 \text{ pc}$, the mapping observation of multiple optically thick molecular line could still be useful to give evidence to large scale infall signatures in dense cores. Six infall candidates were identified in our mapping observations, in which large

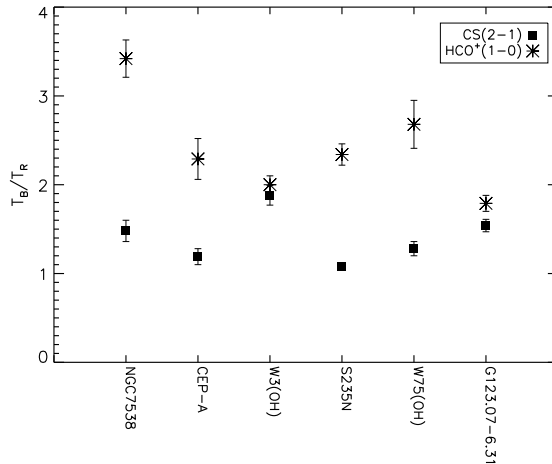


Figure 9. Intensity ratios T_B/T_R in $\text{HCO}^+(1-0)$ and $\text{CS}(2-1)$ for the six infall candidates.

scale ($> 0.2 \text{ pc}$) infall signatures were detected. Among them, NGC7538 has been previously well studied by Sandell et al. (2005). Their high resolution BIMA $\text{HCO}^+(1-0)$ observation suggests that an embedded protostar embedded in the core is still in a phase of active accretion. All these might suggest that large scale infall motions are closely related to the kinematics of the inner materials of the cores. A large scale infall might play a certain role in providing some materials for the innermost accretion.

Actually, outflow makes an important contribution to the line wing emissions. But high quality spectra of much higher signal-to-noise ratios are needed to make better judgement in line wings. Following previous similar studies and our observational results, we here believe that the line asymmetry is mainly contributed by infall motion. And to a certain extent, large scale infall signature at least provides an indirect evidence for the inner accretion. Protostellar accretion could be the main physical process responsible for massive star formation. Some models suggest that the accretion must halt before a visible UC HII phase (eg. Garay & Lizano 1999), while other models suggest that an ionized accretion can continue through an HII region (eg. Keto 2003). Four out of our six infall candidates have already formed UC HII region (W3(OH), CEP-A, NGC7538) and HII region (G123.07-6.31), yet they still show large scale infall signatures. Although we don't know whether infall motions halt at smaller scale of the cores, these examples at least at large scale appeared to be consistent with the ionized accretion theory of Keto (2003).

Comparing with other surveys, our observations show only two (8%) red asymmetry detection in $\text{CS}(2-1)$ and no red asymmetry detection in $\text{HCO}^+(1-0)$ (vs. 21% in $\text{HCN}(3-2)$ observation of Wu & Evans (2003); 16% in $\text{HCO}^+(1-0)$ observation of Fuller et al. (2005); 10% in $\text{HCO}^+(1-0)$ of Wu et al. (2008)). The likely reason is beam dilution and/or the fact that the samples of all surveys until now are still rather limited (typically ~ 30 , e.g., 28 sources of Wu & Evans (2003); 23 sources of Klaassen & Wilson (2007), vs. 77 sources of Fuller et al. (2005)). Of course, these are just some face values and the exact percentage should be affected by resolution. But it is rather arbitrary to scale the

resolution in comparing to other observations. S87 is such an interesting source which shows different asymmetry in CS(2-1) and HCO⁺(1-0) at different offsets (so might be G35.20-0.74). With our telescope resolving power, it's hard to give a reasonable explanation for the different asymmetry in different positions. The possible explanation also include cloud-cloud collision (e.g. S87, Xue & Wu 2008). Oscillating was also suggested in some low mass cores, e.g., B68 (Redman et al. 2006) and perhaps this might be possible in these massive cores as well. High resolution observations are required towards these sources in order to learn more details about the kinematics of massive star-forming cores. Unlike blue profile, the origin of red profile is still unclear. A simple explanation is that the red profile could be caused by outward motions.

5 SUMMARY

We performed a systematic multiple transition 3 mm molecular line single-pointing and mapping survey towards 29 massive star-forming cores to search for the signatures of the inward motions. Up to seven different transitions, optically thick lines HCO⁺(1-0), CS(2-1), HNC(1-0), HCN(1-0), ¹²CO(1-0) and optically thin lines C¹⁸O(1-0), ¹³CO(1-0) were observed towards each source. The major results found from these observations include the following:

(i) The normalized velocity differences (δV_{CS} , δV_{HCO^+}) between the peak velocities of optically thick lines and optically thin C¹⁸O(1-0) for each source were derived. We found a significant difference in the incidence of blue-shifted line asymmetry between CS(2-1) and HCO⁺(1-0). The HCO⁺(1-0) line shows the highest occurrence of obvious asymmetric feature. The optical depth difference between the two molecular lines may be responsible for the anomaly. HCO⁺(1-0) line appears to be one of the best inward motion tracers in massive cores whereas CS(2-1) is not a sensitive tracer to signify the infall motion.

(ii) Blue profile dominance appeared in both CS(2-1) and HCO⁺(1-0) in most of our sample. This implies the predominance of the inward motion in the massive star-forming cores, which is similar to that in low mass star forming regions. All those may suggest that protostellar accretion could be the main physical process responsible for massive star formation.

(iii) The mapping observations of multiple line transitions enable us to identify six strong infall candidates (G123.07-6.31, W75(OH), S235N, CEP-A, W3(OH), NGC7538). Signatures of extended inward motions are presented in these massive star-forming cores with possibly strong infall. The infall signature is extended up to a linear scale > 0.2 pc.

ACKNOWLEDGMENTS

We are grateful to all staff of the 14 m telescope of Purple Mountain Observatory for their dedicated assistance, H.J. Ma for the use of her FCRAO data. We thank Profs. J.Z. Wang, X.Z. Zheng, & Y.F. Wu, Dr. J.W. Wu, and Mr. M. Fang for useful discussions. We also thank the anonymous referee for a very helpful report and comments that help improved the paper. Research for this project is supported

by NSFC Distinguished Young Scholars (#10425313) and Chinese Academy of Sciences' Hundred Talent Program.

REFERENCES

- Allen L.E., Hora J.L., Megeath S.T., Deutsch L.K., Fazio G.G., Chavarria L., Dell R.W. 2005, IAUS, 227, 352
 Beuther H., Schilke P., Menten K.M., Motte F., Sridharan T.K., Wyrowski F., 2002, ApJ, 566, 945
 Beltrán M.T., Cesaroni R., Codella C., Testi L., Furuya R.S., Olmi L., 2006, Nat, 443, 427
 Bonnell I.A., Bate M.R., Zinnecker H., 1998, MNRAS, 298, 93
 Bonnell I.A., Bate M.R., 2006, MNRAS, 370, 488
 Carral P., Kurtz S., Rodriguez L.F., Mart J., Lizano S., Osorio M., 1999, RMxAA, 35, 97
 Dickel H.R., Auer L.H., 1994, ApJ, 437, 222
 Eiroa C., Elasser H., Lahulla J.F., 1979, A&A, 74, 89
 Evans N.J., 1999, ARAA, 37, 311
 Evans N.J., 2003, in Chemistry as a Diagnostic of Star Formation, eds. C.L. Curry & M. Fich, NRC Press, Ottawa, Canada, 2003, p. 157.
 Evans N.J., II, Beichman C., Gatley I., Harvey P., Nadeau D., Sellgren K., 1981, ApJ, 246, 409
 Fazio, G.G. et al., 2004, ApJS, 154, 10
 Felli M., Testi L., Valdetaro R., Wang J.-J., 1997, A&A, 320, 594
 Felli M., Massi F., Robberto M., Cesaroni R., 2006, A&A, 453, 911
 Fuller G.A., Williams S.J., Sridharan T.K., 2005, A&A, 442, 949
 Garay G., Lizano S., 1999, PASP, 111, 1049
 Gregersen E.M., Evans N.J., II, Mardones D., Myers P.C., 2000, ApJ, 533, 440
 Jiang Z.B., Tamura M., Fukagawa M., 2005, Nat, 437, 112
 Keto E., 2003, ApJ, 599, 1196
 Klaassen P.D., Wilson C.D., 2007, ApJ, 663, 1092
 Krassner J., Pipher J.L., Sharpless S., 1979, A&A, 77, 302
 Krumholz M.R., Bonnell I.A., 2007, astro-ph, 0712, 0828
 Lee C.W., Myers P.C., Tafalla M., 1999, ApJ, 526, 788
 Lee C.W., Myers P.C., Tafalla M., 2001, ApJS, 136, 703
 Lee C.W., Myers P.C., Plume R., 2004, ApJS, 153, 523
 Lee J.-E., Young C.H., Shirley Y.L., Mueller K.E., Evans N.J., II, 2002, ASPC, 267, 377
 Lo K.Y., Burke B.F., Haschick A.D., 1975, ApJ, 202, 81
 Ma H.J., Gao Y., Wu J.W., 2008, in prep.
 Mardones D., Myers P.C., 1997, ApJ, 489, 719
 Moscadelli L., Cesaroni R., 2005, A&A, 438, 889
 Myers P.C., Mardones D., 1996, ApJ, 465, 133
 Redman M.P., Keto E., Rawlings J.M.C., 2006, MNRAS, 370, 1
 Ridge N.A., Wilson T.L., Megeath S.T., Allen L.E., Myers P.C., 2003, AJ, 126, 286
 Rieke, G.H. et al., 2004, ApJS, 154, 25
 Sandell G., Goss W.M., Wright M., 2005, ApJ, 621, 839
 Shirley Y.L., Evans N.J., II, Young K.E., Knez C., Jaffe D.T., 2003, ApJ, 149, 375
 Shu F.H., 1977, ApJ, 214, 488
 Shu F.H., Adams F.C., Lizano S., 1987, ARA&A, 25, 23
 Sohn J., Lee C. W., Park Y.-S., Lee H.M., Myers P.C., Lee Y., 2007, ApJ, 664, 928

- Tofani G., Felli M., Taylor G.B., Hunter T.R., 1995, *A&AS*, 112, 299
- Tsamis Y.G., Rawlings J.M.C., Yates J.A., Viti S., 2008, *astro-ph*, 0803, 0519
- Welch W.J., Dreher J.W., Jackson J.M., 1988, *Sci*, 238, 1550
- Whitney B.A., 2005, *Nat*, 437, 37
- Wolf-Chase G.A., Gregersen E., 1997, *ApJ*, 479, L67
- Wu J.W., Evans N.J., II, 2003, *ApJ*, 592, L79
- Wu Y.F., Henkel C., Xue R., Guan X., Miller M., 2007, *ApJ*, 669, L37
- Wu Y.F., Zhu M., Wei Y., 2005, *ApJ*, 628, L57
- Xu Y., Reid M.J., Zheng X.W., Menten K.M., 2006, *Sci*, 311, 54
- Xu Y., Reid M.J., Menten K.M., Brunthaler A., Zheng X.W., Moscadelli L., 2007, *IAUS*, 242, 374
- Xue R., Wu Y.F., 2008, *ApJ*, 680, 446
- Zhang Q., Ho P.T.P., Ohashi N., 1998, *ApJ*, 494, 636
- Zhang Q., Hunter T.R., Brand J., 2001, *ApJ*, 552, L167
- Zhou S., Evans N.J., II, Koempe C., Walmsley C.M., 1993, *ApJ*, 404, 232
- Zhou S., Evans N.J., II, Koempe C., Walmsley C.M., 1994, *ApJ*, 421, 854

APPENDIX A: IRAC AND CO LINE COMPARISON IN S235

The recently available high-resolution and very sensitive mid-infrared and far-infrared images of the Spitzer telescope can provide a new insight in directly locating the distribution of dust obscured massive stars in the dense cores. As an example for some well studied dense core sources, we here compare our molecular line observations with the Spitzer IRAC images in S235. The Spitzer IRAC data were retrieved from Spitzer Science Center¹. IRAC 4 bands data of S235 (PI G. Fazio, PID=201) covering $\sim 0.25 \text{ deg}^2$ reveal a complex star-forming region.

The S235 star-forming region is a well known HII region that has been widely studied. It has been identified as a water maser (Lo, Burke, & Haschick 1975) with infrared (e.g. Krassner, Pipher & Sharpless 1979; Felli et al. 1997; Allen et al. 2005), radio continuum (Felli et al. 1997, 2006), dust continuum emission (Lee, Young & Shirley 2002), and many molecular line emission (e.g. Evans et al. 1981; Felli et al. 1997; Lee, Young, & Shirley 2002).

Our CO maps show that three $^{13}\text{CO}(1-0)$ cores are well matched with three infrared emission regions in Figure A1. We observed several points in these three cores in CS(2-1) and $\text{HCO}^+(1-0)$, only $\text{HCO}^+(1-0)$ show obvious blue profile around position (6', 2') marked dash open circle. Class I and class II sources in S235 were identified by Allen et al. 2005, and their results show that few YSOs are distributed in the North-West extended core and only two class I sources are distributed around position (6', 2'), whereas many more YSOs are distributed in the other two cores. All these may imply that the region around position (6', 2') is still on the very early stage of star formation.

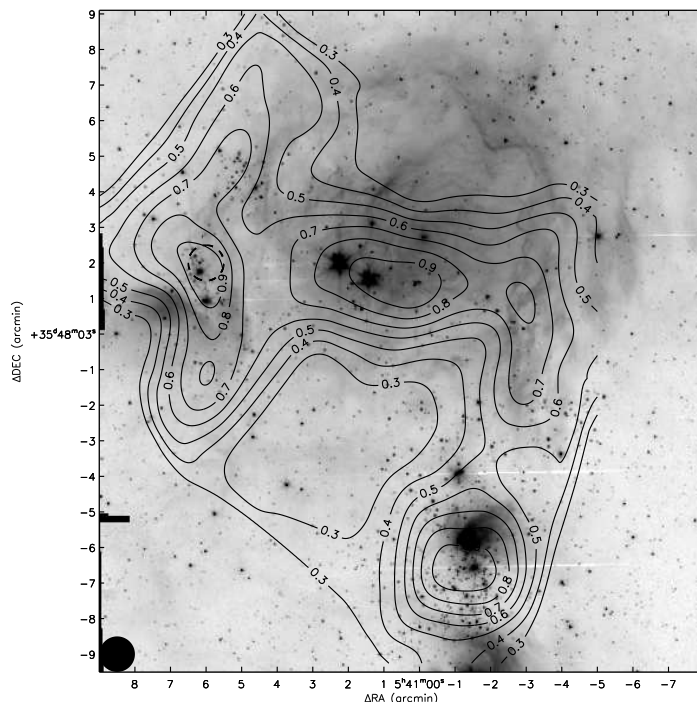


Figure A1. The $^{13}\text{CO}(1-0)$ contour map overlaid on the Spitzer IRAC $4.5 \mu\text{m}$ mosaic of S235. Contour levels start at 30% of the peak $^{13}\text{CO}(1-0)$ integrated intensity and increase by 10% at each interval.

¹ <http://ssc.spitzer.caltech.edu>